**Non-linear astrochemical kinetics: theory and applications**
Dufour, G.C.

**Citation**

Dufour, G. C. (2022, June 21). *Non-linear astrochemical kinetics: theory and applications*. Retrieved from https://hdl.handle.net/1887/3421318

# 5

# THE COMPOSITION OF ICE MANTLES IN DARK CLOUDS: STOCHASTIC SIMULATIONS OF GAS-GRAIN CHEMISTRY

## Abstract

New theoretical and experimental information on solid state astrochemical reaction networks and the involved rate constants have become available recently. This new data is gathered in an extended astrochemical model, based on Charnley et al. 1998 and 2001, with a specific focus on the carbon chemistry of smaller species as these play a key role in the formation of larger carbon bearing species. The results are linked to recent astronomical observations of dense cloud environments. The primary goal of this work is to update the surface chemistry network in a dense cloud environment by performing a sensitivity analysis of an extended grain surface reaction network, and to provide an optimized model. A kinetic Monte Carlo model is used, based on stationary stochastic simulation techniques including both gas and grain chemical evolution. The formation of ice monolayers is included. The reaction H+HCO, which forms CO and $H_2CO$, is found to strongly impact the amount of CO available in the system, which subsequently regulates the amount of $CH_3OH$. We show that $CH_3$+OH is the main formation pathway of methanol before CO freezes-out in the optimized model.

## 5.1 Introduction

The interstellar medium (ISM) contains different environments showing large ranges in temperature and densities. It is filled mainly with hydrogen gas, about 10% helium atoms, and 0.1% of atoms such as C, N, and O. Roughly 1% of the mass is contained in microscopic dust grains. About 240 molecules have been identified in interstellar space, from the smallest carbon-bearing molecule $CH^+$ (Methylidynium, Douglas & Herzberg (1941)) to the biggest and most complex species such as $CH_3COCH_2OH$ (Hydroxyacetone, Zhou et al. (2020)) and $C_{70}$ (Fullerenes, Cami et al. (2010)). For an overview see McGuire (2018). A common way to consider the formation and evolution of larger carbon-bearing species is through the study of so-called complex organic molecules (COMs) and polycyclic aromatic hydrocarbons (PAHs). In this paper we will focus on COMs.

COMs are roughly defined as molecules with six or more atoms that contain at least carbon and hydrogen, typically of the form $C_kH_lX_mY_n$ with X,Y = O, N, S, P. Gas phase spectra of COMs have been observed in a range of interstellar environments (Herbst & van Dishoeck (2009); Belloche et al. (2013); van Gelder et al. (2020)). These molecules have been generally identified in the gas-phase, and in the solid state the only COM found so far is methanol ($CH_3OH$, Boogert et al. (2015)). With the James Webb Space Telescope (JWST), more detailed infrared observations in the solid-state are expected within the framework of a number of General Observer (GO), Guaranteed Time Observations (GTO) and Early Release Science (ERS) programs. For example, the IceAge Early Release Science (ERS) JWST program will search for characteristic vibrational modes or functional groups of complex organic molecules that could not be detected before largely due to sensitivity limitations with ground-based telescopes (McClure et al. (2017); Terwisscha van Scheltinga et al. (2018); Rachid et al. (2020)). These COMs are expected to be present in the ice, as laboratory and theoretical investigations have found that COMs can be formed during the dark cloud stage in the solid-state at interstellar grain temperatures, typically starting from CO hydrogenation involving radical recombinations (Chuang et al. (2016); Butscher et al. (2017); Fedoseev et al. (2017); Álvarez-Barcia et al. (2018); Lamberts et al. (2019)) or from direct carbon addition reactions (Charnley (1997, 1998, 2001); Charnley & Rodgers (2005, 2009); Qasim et al. (2020a); Krasnokutski et al. (2017); Molpeceres et al. (2021)). At later stages, when Ultra-Violet (UV) irradiation plays a role, COMs were also shown to form, e.g. upon energetic processing of methanol (Öberg et al. (2009); Paardekooper et al. (2016)) or the N-equivalent, acetonitrile (Bulak et al. (2020)). Also electron or cosmic rays impacting on interstellar ice analogues were shown to result in a remarkably large molecular complexity (Rothard et al. (2017); Arumainayagam et al. (2019)). Other studies have proposed low temperature gas-phase formation routes as a primary source of COMs. In such cases, simple mantle species are non-thermally desorbed, followed by more complex gas-phase chemistry (Vasyunin & Herbst (2013); Balucani et al. (2015); Codella et al. (2020)).

Solid-state carbon addition routes, which have been less studied than molecular radical-radical reactions, may be important to COM formation during the early period of ice formation, when the atomic carbon abundance is high (Kim et al. (2003)). When the cloud ages, CO becomes the main carrier of carbon, and hydrogenation reactions together with radical-radical reactions are expected to be important to COM formation. If we consider the simplest COM, $CH_3OH$, it is generally accepted that $CH_3OH$ formation is most efficient by solid-state interactions in CO-rich ices through sequential hydrogenation of CO (Hiraoka et al. (1994); Watanabe & Kouchi (2002); Fuchs et al. (2009)). This is further supported by astrochemical models (Cuppen et al. (2009); Garrod et al. (2006)) that show that hydrogenation of CO ice leads to efficient production of $CH_3OH$. This finding is also in line with astronomical observations that show that methanol resides in a CO rich and $H_2O$ poor ice environment (Cuppen et al. (2011)). Moreover, this is in line with observations by Chu et al. (2020) and Booth et al. (2021), where it is shown that a disk around a young, luminous A-type star, likely inherited $CH_3OH$ ice from an earlier cold dark cloud phase. Similarly, it is shown that COMs under translucent cloud conditions can be made via radical-radical reactions (Tielens (1992); Hiraoka et al. (2000); Kobayashi et al. (2017); Qasim et al. (2019a); Chuang et al. (2020)). Considering the earlier stages where C-atoms are more abundant, other methanol formation routes can be at play. For instance, Lamberts et al. (2017) and Qasim et al. (2018) showed that $CH_3OH$ can be formed from the sequential reactions, $CH_4+OH \rightarrow CH_3+H_2O$ and $CH_3+OH \rightarrow CH_3OH$. This latter reaction was also studied in detail by Lamberts et al. (2017).

Furthermore, we have an increase of experimental data on the various reactions occurring on the surface of the icy grains. Recently C-atom beam setup have been introduced (Ioppolo et al. (2013); Krasnokutski et al. (2017); Qasim et al. (2020a,b)). They show that C-atoms are very reactive and eagerly interacts not only with other atoms and radicals on the surface, but even with the stable molecules such as $H_2O$, CO, $CO_2$, $O_2$, $H_2$, etc. (Qasim et al. (2020b); Molpeceres et al. (2021); Lamberts et al. (2021, submitted); Fedoseev et al. (2021, accepted)). This means that the outcome of C-atom reactivity upon accretion on the grains strongly depends on the composition of the upper layer of the ice at any given moment. Thus, we need dedicated models that treat the upper layer as a separate phase because it is particularly important to proper account for the chemical process occurring early in translucent and dark clouds. Therefore in this study, we implement the routes mentioned above, explicitly taking into account C-atom addition reactions, along with recent experimental and theoretical studies, in a "three-phase" (gas phase, ice-surface, ice-mantle) Monte Carlo astrochemical model.

To this end, we (i) update the carbon atom surface chemistry included in a Monte Carlo model; (ii) perform a sensitivity analysis of the grain surface reactions, (iii) provide an optimized model, and (iv) indicate the direction for future models for similar environment. More explicitly, we describe in Section 5.2 the modifications made to the model from which this study starts and how ice chemistry is included. The results in Section 5.3 describe the so-called "Standard model", followed by a sensitiv-

ity analysis and discussion of optimized models. Finally in Section 5.4, we compare
the predicted mantle compositions with existing observations, specifically for CO and
$CH_3OH$, and briefly discuss future ice observations with JWST.

## 5.2   Methods

To correctly calculate the surface chemistry occurring on interstellar dust grains, one
needs to solve the master equation for the surface particle populations. From the the-
ory of continuous-time Markov processes, the master equation assumes that the future
state of a system depends only on its current state. Given their general complexity,
simulation methods are required to solve master equations arising from chemical re-
action systems (e.g. Gillespie (1976, 2005); Weber & Frey (2017)).

To study catalytic chemical reactions, including processes of adsorption, desorp-
tion, diffusion and reaction, both Gillespie's stochastic simulation algorithm (SSA)
(Jansen (1995)) and kinetic Monte Carlo (kMC) simulations can be employed (Cup-
pen et al. (2013)). In the limit of fast surface diffusion, as occurs on interstellar grains,
the SSA and lattice kMC approaches are formally equivalent (Stamatakis & Vlachos
(2011)).

### 5.2.1   Theory

A stochastic treatment of both the gas and the grain-surface chemical kinetics is sug-
gested to calculate the evolving molecular composition of interstellar ice mantles. The
Gillespie algorithm (Gillespie (1976, 2005, 2007)) has been the basis of previous work
(Charnley (1998, 2001); Cuppen et al. (2009); Lamberts et al. (2014)). In the stochas-
tic simulation, the total reactive population of a chemical species, $i$, is $Z_i = Y_i + X_i$,
where $Y_i$ and $X_i$ are independently-distributed random variables representing the in-
stantaneous populations in the gas and on the grain surface. In the present work, the
simulations are performed by combining two stochastic models: one for gas-phase
chemistry (Charnley (1998)) and one for treating surface reactions (Charnley (2001));
this essentially solves the chemical master equation for the combined gas-grain sys-
tem. This approach was also adopted by Vasyunin et al. (2009); Charnley & Rodgers
(2009) and Chang & Herbst (2012). Alternative treatments have employed determin-
istic rate equations for the gas chemical evolution (Chang et al. (2007)).

For the gas-phase, the chemical state is represented by the population vector
$\mathbf{y} = \{Y_i\}$ for $i = 1, 2, ... N_g$ species, connected by $M_g$ reactions, including uni-
molecular and bi-molecular processes, that take place in some reaction volume $V$.
The particle number density of $i$ in the gas is then given by $n_i = <Y_i>/V$ where
$<Y_i>$ is the average population.

Gaseous atoms and molecules collide and stick to the surface of a dust grain where
they can undergo subsequent chemical reactions. This gives rise to an instantaneous
population of species on the dust surface, described by population vector $\mathbf{x} = \{X_i\}$
for $i = 1, 2, ... N_d$. Defining the joint probability distribution function, $P(\mathbf{x}; t)$, as the

probability that the surface is in state $\{X_i\}$ at time $t$, the associated master equation specifically for the surface chemistry, involving $N_d$ chemical species connected by $M_d$ chemical reactions, is

$$\frac{\partial}{\partial t}P(\mathbf{x};t) = \sum_{\mu}^{M_d}\Big[W_{\mu}(\mathbf{x}-\mathbf{s}_{\mu})P(\mathbf{x}-\mathbf{s}_{\mu};t) - W_{\mu}(\mathbf{x})P(\mathbf{x};t)\Big] \qquad (5.1)$$

The state transition rate $W_{\mu}(\mathbf{x})$ is the probability per unit time of process $\mu$ occurring in the infinitesimal time interval $[t, t + dt]$, given that it is in state $\mathbf{x}$ at time $t$. The stoichiometry of reaction $\mu$ is accounted for by the vector $\mathbf{s}_{\mu}$.

The $W_{\mu}(\mathbf{x})$ rates for grain-surface processes are defined as follows. The driving process is accretion of gas phase particles on the grain surface; this is effectively a uni-molecular process that changes the gas and surface populations by $Y_i \longrightarrow Y_i - 1$ and $X_i \longrightarrow X_i + 1$, respectively. Assuming a Maxwellian velocity distribution, and unit sticking efficiency, gas particles collide and stick to a single spherical grain of radius $a$ located within $V$ at a rate

$$W_{\mu}(\mathbf{x})dt = (\frac{8kT}{\pi M_i m_H})^{1/2}\pi a^2 Y_i(t)V^{-1}dt \qquad (5.2)$$

where $T$ is the temperature, $M_i$ is the molecular weight and $k$ is the Boltzmann constant. For $a = 0.1\ \mu$m, $T \approx 10$ K, and $n = 2.0\times10^4$ cm$^{-3}$, one has

$$W_{\mu}(\mathbf{x})dt \approx 10^{-5}M_i^{-1/2}Y_i(t)V^{-1}dt. \qquad (5.3)$$

Atoms and molecules can also desorb from the surface monolayer by a number of processes. In the present study, desorption is inefficient as a result of the low temperature, except for thermal desorption of atomic H, C and O and the evaporation of $H_2$ directly after formation (see Section 5.2.3). We also assume that when $H_2$ is formed via another reaction other than H + H, the molecule is desorbed into the gas phase. We do not include reactive desorption (Garrod et al. (2006); Minissale et al. (2016a); Chuang et al. (2018); Oba et al. (2018)).

For a surface reaction between two distinct species $i$ and $j$, the associated transition rate $W_{\mu}(\mathbf{x})$ can be written as

$$W_{\mu}(\mathbf{x})dt = \gamma_{\mu}q_{\mu}(\mathbf{x})p_{\mu}dt \qquad \mu = 1, 2, ..., M_d \qquad (5.4)$$

The number of particles available for chemical reactions is constrained by the maximum number that can be accommodated in the surface monolayer binding sites. Estimates suggest that a refractory grain core will contain $\mathcal{N} = 10^6$ binding sites (e.g. Tielens & Allamandola (1987)). Particles can - in principle - move on the surface by quantum tunnelling or thermal hopping. The stochastic surface rate coefficient, $\gamma_{\mu}$, is given by $\tau_{\mu}^{-1}$, the inverse of the characteristic time-scale for a particle to move to an adjacent surface site by either process (see Section 5.2.3). The probability factor $p_{\mu}$, allows reactions with activation-energy barriers to be treated. For tunneling processes,

simple analytic approximations can be used for $p_\mu$ (e.g. Charnley (2001)). However, in this study we instead use reaction rates from the quantum chemistry literature that have been directly computed for each specific process.

For thermal processes,

$$p_\mu = \exp(-\frac{E_b}{RT}) \tag{5.5}$$

where $E_b$ is the energy barrier and $R$ is the gas constant. For no barrier $p_\mu = 1$. The combinatorial factor $q_\mu(\mathbf{x})$ accounts for the number of distinct ways two species, having surface populations $X_i$ and $X_j$, can react on a surface with a finite number of binding sites $\mathcal{N}$. This is the number of ways an $i + j$ pair can be selected from the instantaneous distribution of surface particles, whose total is $\mathcal{N}$; we adopt $q_\mu(\mathbf{x}) = X_i X_j / \mathcal{N}(\mathcal{N} - 1)$ and assume $\mathcal{N} = 10^6$ for all ice monolayers. It is assumed that only the surface of the mantle is chemically active. In this implementation of the Gillespie stochastic algorithm, the simulation event that changes the surface state of the system is a chemical reaction, including accretion and desorption (see also Vasyunin et al. (2009)). This is the well-mixed description of stochastic kinetics. Particle diffusion is not treated explicitly and would require performing simulations on a defined lattice structure (e.g. Chang et al. (2007); Simons et al. (2020)). In this case the occupancy of each lattice node can be identified with a chemical species (or none) and the next event can be a reaction or migration with no reaction. The well-mixed and lattice-based descriptions are equivalent in the limiting case of fast particle diffusion (Stamatakis & Vlachos (2011)).

Computational implementation of the stochastic simulation for both gas and surface chemistry is straightforward. This simply involves combining the relevant reactions into one list, evaluating the instantaneous $W_\mu(\mathbf{x})$ for each, then selecting the next reaction that occurs through Gillespie's Monte Carlo procedure. In the simulation, mantle growth proceeds one particle at a time. After a monolayer has formed, subsequent accretion and reaction leads to it being covered as the next monolayer forms. Burial removes particles from the instantaneous reactive surface population but chemical reactions and desorption can reveal subsurface particles. Therefore, we keep track of this covering (by accretion) or uncovering (by reaction or desorption) in the simulation by accessing the computed population of the immediate subsurface monolayer. As monolayers are buried, they comprise the *bulk* ice mantle. The composition of each monolayer is monitored to obtain the total population of molecule $i$ in the bulk ice, $X_i^B$.

The simulation code is based on previous stochastic treatments of gas and grain-surface processes (accretion, desorption, tunneling, diffusion), Charnley (1998, 2001). S.B. Charnley used assumptions and approximations on the processes equations that differ from recent investigations (Cuppen et al. (2017); Simons et al. (2020)). These and other differences related to the adopted ice chemistry and their eventual impact are described in the following Sections.

**Table 5.1:** Dense cloud simulation parameters

| | | |
|---|---|---|
| Simulation reaction volume | $V$ | $5.0 \times 10^7$ cm$^3$ |
| Temperature | $T$ | 10 K |
| Density | $n$ | $2 \times 10^4$ cm$^{-3}$ |
| Visual extinction | $A_V$ | 10 mag |
| Cosmic ray ionization rate | $\zeta$ | $5 \times 10^{-17}$ s$^{-1}$ |
| Grain radius | $a$ | 0.1 $\mu$m |
| Elemental abundances: | $X_O$ | $8.53 \times 10^{-5}$ |
| | $X_C$ | $3.62 \times 10^{-5}$ |
| | $X_{He}$ | 0.1 |

### 5.2.2   Gas phase chemistry

The gas phase chemistry is derived from Millar et al. (1997) and is limited to reactions involving carbon, oxygen, hydrogen and helium. These include neutral-neutral and ion-molecule bi-molecular reactions, CR-induced photo-ionization and accretion onto grains. Direct ultraviolet radiation is not considered for our system, i.e. we limit ourselves to the prestellar (dark and dense) phase where non-energetic processing, atom addition reactions, dominate the solid state processes. The chemical network comprises 104 species and 769 reactions. The initial conditions are listed in Table 5.1, and we assume that the gas and grain temperatures are equal. The density and visual extinction of the environment chosen are appropriate for dense clouds (Snow & McCall (2006); Hollenbach et al. (2009)). The gas phase volume is equal to $5 \times 10^7$ cm$^{-3}$, enough for the relatively small species used here. The initial value of the H$_2$/H ratio was taken to be $10^{-4}$. We chose the carbon to be stored in atomic carbon, using initial chemical abundances as outlined in Table 5.1. In agreement with recent observations (Fuente et al. (2019)) we have adopted a C/O ratio of 0.4 and initial conditions similar to earlier models Pineau des Forets et al. (1992); Taquet et al. (2012); Dufour & Charnley (2019).

Under interstellar conditions, the hydrogen atom abundance in the gas phase stays roughly constant as a consequence of the balance between conversion of H to H$_2$ occurring on the surfaces of cold dust grains (Hollenbach & Salpeter (1970, 1971); Takahashi et al. (1999)), and release of H from H$_2$ in gas-phase ion-molecule and ion-electron reactions initiated by cosmic-ray ionization of H$_2$ (Vroom & de Heer (1969)). We applied a branching ratio (BR) of 10% H$_2$ staying on the grain surface and 90% evaporating back into the gas-phase. For the present study, H$_2$ ice chemistry is not taken into account, but it should be noted that reactions involving H$_2$ do occur, as recent experimental and theoretical work shows (Lamberts et al. 2021, submitted).

The gas-phase chemistry evolves over time at 10 K without any UV radiation. In our model, as species freeze out gradually onto the grain, they can react via a combination of thermal diffusion processes and exothermic reactions.

| Index | Reactants | Products | Eb (K) | Eb (kJ.mol-1) | k (s-1) | ref. | ΔBR | | Δk | |
|---|---|---|---|---|---|---|---|---|---|---|
| **Desorption processes** | | | | | | | | | | |
| 1 | H + grain | H-gas | 3.50E+02 | 2.91 | | [1] | | | | |
| 2 | O + grain | O-gas | 1.44E+03 | 11.97 | | [2] | | | | |
| 3 | C + grain | C-gas | 1.41E+04 | 117.23 | | [2] | | | | |
| **Exothermic processes** | | | | | | | | | | |
| 4 | H + O | OH | | | | [3] | | | | |
| 5 | H + OH | $H_2O$ | | | | [3] | | | | |
| 6 | H + H | $H_2$-gas | | | | [3] | | | | |
| 7 | H + $CH_2OH$ | $CH_3OH$ | | | | [4] | | | | |
| 8 | H + $CH_2OH$ | $H_2CO$ + $H_2$ | | | | [4] | | | | |
| 9 | H + C | CH | | | | [5] | | | | |
| 10 | H + CH | $CH_2$ | | | | [5] | | | | |
| 11 | H + $CH_2$ | $CH_3$ | | | | [5] | | | | |
| 12 | H + $CH_3$ | $CH_4$ | | | | [5] | | | | |
| 13 | H + $CH_3O$ | $CH_3OH$ | | | | [4] | | | | |
| 14 | H + $CH_3O$ | $H_2CO$ + $H_2$ | | | | [4] | | | | |
| 15 | H + HCO | CO + $H_2$ | | | | [3] | 0.8 | 0.98 | | |
| 16 | H + HCO | $H_2CO$ | | | | [3] | 0.2 | 0.02 | | |
| 17 | H + HOCO | $CO_2$ + $H_2$ | | | | [6], [7] | 1.0 | 0.0 | | |
| 18 | H + HOCO | HCOOH | | | | [6], [7] | 0.0 | 1.0 | | |
| 19 | H + $O_2$ | $HO_2$ | | | | [3] | | | | |
| 20 | H + $HO_2$ | OH + OH | | | | [3], [8] | | | | |
| 21 | H + $HO_2$ | $H_2O_2$ | | | | [3], [8] | | | | |
| **Thermal Hopping processes** | | | | | | | | | | |
| 22 | O + C | CO | | | | [9] | | | | |
| 23 | O + HCO | $CO_2$ + H | | | | [9] | | | | |
| 24 | O + HCO | CO + OH | | | | [9] | | | | |
| 25 | O + O | $O_2$ | | | | [3] | | | | |
| 26 | C + OH | CO + H | | | | [9], [10] | | | | |
| 27 | C + $O_2$ | CO + O | | | | [11] | 0.0 | 0.5 | | |
| 28 | C + $O_2$ | $CO_2$ | | | | [12], [13] | 1.0 | 0.5 | | |
| 29 | OH + CO | HOCO | | | | [14], [15], [16] | 0.5 | 0.0 | | |
| 30 | OH + CO | $CO_2$ + H | | | | [14], [15], [16] | 0.5 | 1.0 | | |
| 31 | OH + OH | $H_2O_2$ | | | | [17] | | | | |
| 32 | OH + OH | $H_2O$ + O | | | | [17] | | | | |
| 33 | OH + HCO | HCOOH | | | | [6] | 1.0 | | | |
| 34 | OH + HCO | $H_2O$ +CO | | | | [6] | 0.0 | | | |
| 35 | $CH_3$ + OH | $CH_3OH$ | | | | [18], [19] | | | | |
| **Quantum tunneling processes** | | Ea (K) | Ea (kJ.mol-1) | k (s-1) | | | | | | |
| 36 | H + CO | HCO | 1.85E+03 | 15.3 | 2.00E+05 | [12], [13] | | | 5.0E+04 | 5.0E+05 |
| 37 | H + $H_2CO$ | HCO + $H_2$ | 2.47E+03 | 20.5 | 7.00E+05 | [13] | | | 1.0E+05 | 1.0E+06 |
| 38 | H + $H_2CO$ | $CH_3O$ | 2.16E+03 | 18.0 | 1.30E+06 | [20] | | | 5.0E+05 | 5.0E+06 |
| 39 | H + $H_2CO$ | $CH_2OH$ | 5.21E+03 | 43.3 | 7.00E+01 | [20] | | | | |
| 40 | H + $CH_3OH$ | $CH_2OH$ + $H_2$ | 3.61E+03 | 30.0 | 7.00E+03 | [21] | | | 1.0E+03 | 5.0E+04 |
| 41 | H + $CH_3OH$ | $CH_3O$ + $H_2$ | 5.53E+03 | 46.0 | 2.00E+01 | [3] | | | | |
| 42 | H + $H_2O_2$ | $H_2O$ + OH | 2.53E+03 | 21.0 | 2.00E+05 | [22], [23] | | | | |
| 43 | H + $H_2O_2$ | $HO_2$ + $H_2$ | 3.26E+03 | 27.1 | 2.00E+01 | [22], [23] | | | | |
| 44 | $H_2$ + OH | $H_2O$ + H | 3.00E+03 | 24.9 | 4.50E+05 | [24] | | | | |
| **Thermal Activation processes** | | | | | | | | | | |
| 45 | CO + O | $CO_2$ | 2.97E+03 | 24.7 | 1.00E-12 | [25] | | | | |
| 46 | C + $CO_2$ | CO + CO | 3.51E+03 | 29.2 | - | [11] | | | 1.0E+00 | |
| 47 | OH + HOCO | $H_2O$ + $CO_2$ | - | - | 1.00E+10 | [16] | | | | |
| 48 | OH + $H_2CO$ | $H_2O$ + HCO | 1.92E+03 | 16.0 | 1.00E+06 | [26], [27], [28] | | | | |
| 49 | $CH_4$ + OH | $CH_3$ + $H_2O$ | - | - | 4.00E+03 | [29] | | | | |
| 50 | $CH_3O$ + $H_2CO$ | $CH_3OH$ + HCO | - | - | 2.00E+03 | [3] | | | | |
| 51 | OH + $CH_3OH$ | $H_2O$ + $CH_2OH$ | 2.25E+03 | 18.7 | 2.00E+06 | [30], [31], [32], [33] | | | | |
| 52 | OH + $CH_3OH$ | $H_2O$ + $CH_3O$ | 3.16E+03 | 26.3 | 5.00E+06 | [30], [31], [32], [33] | | | | |

**Table 5.2:** Updated surface chemistry for a cold and dense environment. ▫ Reactions studied during the Sensitivity analysis. ▪ Reactions added during the Sensitivity analysis. List of references: [1] Tielens & Allamandola (1987), [2] Shimonishi et al. (2018), [3] Simons et al. (2020), [4] Qasim et al. (2020a), [5] Qasim et al. (2019b), [6] Goumans et al. (2008), [7] Tielens & Hagen (1982), [8] Lamberts et al. (2014), [9] Prasad & Huntress (1980), [10] Zanchet et al. (2006), [11] Qasim et al. (2020b), [12] Andersson et al. (2011), [13] Álvarez-Barcia et al. (2018), [14] Nguyen et al. (2012), [15] Masunov et al. (2016), [16] Taquet et al. (2016), [17] Lamberts et al. (2014), [18] Qasim et al. (2018), [19] Walch (1993), [20] Song & Kästner (2017), [21] Cooper & Kästner (2019), [22] Lamberts et al. (2016), [23] Lamberts & Kästner (2017), [24] Meisner et al. (2017), [25] Goumans & Andersson (2010), [26] Zanchet et al. (2018), [27] Naumkin et al. (2019), [28] Mazo-Sevillano et al. (2021), [29] Lamberts et al. (2017), [30] Nguyen et al. (2019), [31] Roncero et al. (2018), [32] Ocaña et al. (2019), [33] Shannon et al. (2013).

### 5.2.3   Grain surface chemistry

We built a surface chemistry network with updated rate constants, activation energies, and branching ratios. Table 5.2 shows in detail the surface reactions used in this study with the references listed. The Standard model includes processes 1 – 46, excluding 35. For the sensitivity analysis, rate constants and branching ratios (BR) of reactions 15-16, 17-18, 27 – 30, 33-34, 36 – 38, 40 and 46 have been varied (gray highlighted reactions) along with reactions 35, 47 – 52 being added (green highlighted reactions). Finally, the optimized model includes all reactions listed in Table 5.2. [1]

We define the stochastic rate coefficients for surface processes, $\gamma_\mu$ (Eqn. 5.4 ), through their associated timescales, $\tau_\mu$: for hydrogen tunnelling and thermal hopping these are $\tau_H$ and $\tau_{HOP}$. The rate of a two-body surface reaction is effectively determined by the largest value of $\gamma_\mu$ between the two reactants.

Recent calculations using an accurate potential, indicate that hydrogen atoms atop $H_2O$ ice migrate on a characteristic timescale of $\tau_H = 10^{-11}$ s (Senevirathne et al. (2017); Ásgeirsson et al. (2017)). Heavier particles move by thermal hopping on a timescale

$$\tau_{HOP} = \nu^{-1}\exp(\frac{E_D}{kT_d})  \qquad (5.6)$$

where $T_d$ is the grain surface temperature, $E_D$ is the energy barrier for surface diffusion, and $\nu$ is the vibrational frequency of the particle in a surface binding site. For $\nu$ we used a similar value to that of Simons et al. (2020), of $2.0\times10^{11}$ s$^{-1}$. The value of $E_D$ is usually taken as a fraction of the binding energy for physisorption, $E_B$, such that

$$E_D = \epsilon E_B  \qquad (5.7)$$

---

[1]The most abundant reactive species arriving from the gas are atomic H, C and O. Table 5.2 also lists their adopted binding energies, as adsorption energies, taken from a recent theoretical study by Shimonishi et al. (2018); clearly only H atoms can undergo thermal desorption.

with $\epsilon \approx 0.3 - 0.5$ (Cuppen et al. (2013)), and assumed to be the same for all surface species. Following previous work (e.g. Tielens & Hagen (1982)) and recent experiments (Kouchi et al. (2020)), in this study we employ $\epsilon = 0.3$.

In this study we have adopted a single value of $\gamma_{\text{HOP}}$ for the most reactive radical species in the network of Table 5.2 : O, C and OH. Because of the exponential dependence in equation (5.6), uncertainties in $E_B$ and $\epsilon$ can have a dramatic effect on on the derived value of $\tau_{\text{HOP}}$. In our model, $E_D = 240$ K, as in Charnley (2001) and Caselli et al. (1998), yielding $\tau_{\text{HOP}} = 0.13$s. This is based on an estimate of $E_B = 800$K for O, C and N atoms, derived from simple polarizability arguments (e.g. Tielens & Allamandola (1987)).

Previous models of surface chemistry have typically considered two general cases. The case when only atoms are assumed to be mobile on the surface with all other species relatively static (e.g. Tielens & Hagen (1982)), or when, in addition, all heavy molecular species can diffuse by hopping according to their specific $E_D$, as estimated above (e.g. Garrod (2013)).

Our assumption of a single and rapid $\tau_{\text{HOP}}$ for the network of Table 5.2 can be justified based on recent experimental and theoretical work on the relevant values of $E_B$.

For atomic oxygen binding to amorphous water surface (ASW), both experiment and theory suggest $E_B \approx 1400$K (Minissale et al. (2016b); Shimonishi et al. (2018)). This would lead to $\tau_{\text{HOP}} = 8.7 \times 10^6$s for $\epsilon = 0.3$ and $7.9 \times 10^3$s for $\epsilon = 0.25$. The important general point is that for $E_B \lesssim 1300$K thermal hopping can be rapid, whereas much above this value a surface particle will be static.

On the other hand, calculations indicate that atomic carbon binds to ASW by chemisorption (Shimonishi et al. (2018)). The correspondingly large binding energy, $E_B = 14,100$K and $\tau_{\text{HOP}}$ renders C atoms immobile with respect to thermal hopping. However, the main co-reactants of atomic carbon in Table 5.2 can plausibly have $\tau_{\text{HOP}}$ in the desired range. Measurements of $O_2$ binding on ASW suggest $E_B \approx 1000 - 1200$K (Hama & Watanabe (2013); Minissale et al. (2016b)) and hence that reactions (27) and (28) will proceed efficiently.

The diffusion of OH radicals at low temperatures is more uncertain. Experimental determinations of OH on silicate surface and water ice surfaces yield $E_B = 4600$K (Dulieu et al. (2013); Minissale et al. (2016b)). Theoretical calculations of OH binding to ASW (Ferrero et al. (2020)) predict a range of values $E_B \approx 1550 - 5321$K depending on the amorphous structure of the ice. Adopting the lower value of $E_B$ (and the caveat that $\epsilon \approx 0.25$) could yield a $\tau_{\text{HOP}}$ comparable to that assumed here. We note also that binding energy estimates of several OH co-reactants in Table 5.2, CO ($E_B \approx 1100 - 1180$K, Collings et al. (2003); Penteado et al. (2017)), $CH_3$ and HCO (Penteado et al. (2017); Ferrero et al. (2020)) could allow OH reactions with these species to occur irrespective of OH mobility.

In conclusion, if individual binding energies are considered for the reactants in Table 5.2, we estimate that all reactions take place with at least one reactant having a sufficiently short $\tau_\mu$.
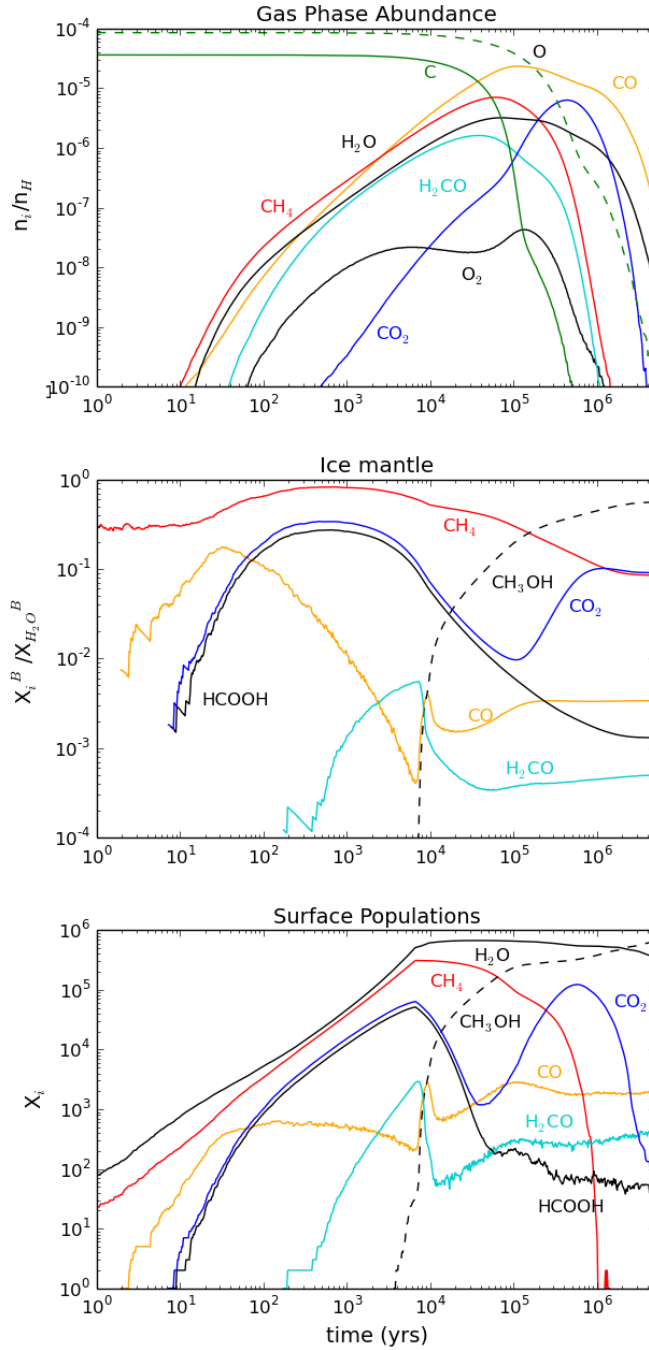
**Figure 5.1:** Evolution of the most abundant species in the Standard model simulation. Top panel: gas-phase fractional abundances relative to hydrogen. Middle panel: molecule abundances in the bulk ice mantle relative to $H_2O$. Bottom panel: molecule populations on the grain surface.

## 5.3 Results & Discussion

### 5.3.1 Standard model

The surface chemistry created for the Standard model includes formation of the principal molecules: $H_2O$, $CH_4$, $CO_2$, $H_2CO$, HCOOH and $CH_3OH$. The fractional abundances of the molecules in the gas-phase, $n_i/n_H$, are shown in the top panel of Figure 5.1, whereas the fractional abundances in the bulk ice mantle relative to $H_2O$ ice, $X_i^B/X_{H_2O}^B$, are shown in the middle panel. The bottom panel shows the surface population of each species, $X_i$. The gas-phase chemical evolution shows the C-CO transition around $5\times10^4$ years, and shows that O and C are both mainly stored in CO after $5\times10^5$ years. All species begin to freeze-out at ~ $10^4$ years. Concerning the ice chemistry, in this $H_2O$-rich environment, $CH_4$ is the second most abundant species in the mantle and at the surface before $10^5$ years. Afterwards, $CH_3OH$ becomes the second major species in the ice.

From analyzing the chemistry in the Standard model, it is found that the main reactions leading to the formation of the aforementioned molecules are similar to recent conclusions from experimental and theoretical studies and in line with astronomical observations:

- The main formation routes for $H_2O$ are reactions 44 and 5, in agreement with Ioppolo et al. (2010), Oba et al. (2012) and Lamberts et al. (2014).

- Following the early hypothesis of van de Hulst (1946), Öberg et al. (2008, 2011) suggested from observational evidence that the formation of solid $CH_4$ takes place via the hydrogenation of atomic carbon, which was confirmed experimentally by Qasim et al. (2020a). Our reactions 9 – 12 are in agreement with that. Very recent work also shows methane formation starting from $C+H_2$, which will be included in a future study.

- The formation of formaldehyde and methanol through hydrogenation of carbon monoxide (CO) has been demonstrated in laboratory experiments (Watanabe & Kouchi (2002); Fuchs et al. (2009); Hidaka et al. (2004); Chuang et al. (2016, 2017, 2018)). Our reactions 36 and 16 along with 38 and 13 represent the main formation pathways.

- The experiments performed in Ioppolo et al. (2011) and Qasim et al. (2019b) indicate a two-step formation route with OH+CO forming a hydrocarboxyl radical (HOCO), followed by the hydrogenation of HOCO to form HCOOH and $CO_2$ (reaction 29 → 17 and 18).

We can compare our results to similar stochastic grain surface astrochemical models and astronomical observations. Chu et al. (2020), observed a ratio of $CH_3OH_{ice}$/$CO_{pure}$ in a range of 0.45 to 0.49, i.e. $CO_{pure}/CH_3OH$ ~2.0. Boogert et al. (2015) observed a ratio of $CO/CH_3OH$ in a range of <1 to 10<, from LYSOs and MYSOs

environments, as shown in table 5.3. Simons et al. (2020) used a kinetic Monte Carlo model and obtained a higher ratio of $CO/CH_3OH$ equal to ~16 and a ratio of $H_2CO/CH_3OH$ equal to ~3. In our case, $CO/CH_3OH$ ratio varies from 0.02 to 0.007 over time. Thus, Chu et al. (2020) are in the range of previous results observed by Boogert et al. (2015), while Simons et al. (2020) have ratios on the higher hand of the observations results and our results are on the lower hand. Two clear differences with Simons et al. (2020) are how they implemented CO initially in their model and the use of a higher density. They did not include the C-CO transition explicitly, but rather started with a high abundance of CO in the gas-phase, whereas we selected the formation of CO to happen over time. This condition leads to a very different initial CO/H ratio (varying from 1.6 to 10.0 for Simons et al. (2020) and below one for our work), which results in differences in the ice chemistry between the two studies. In Section 5.3.2, to observe the impact on the overall ice chemistry, we test and discuss the results obtained varying the CO/H ratio depending on similar initial conditions of Simons et al. (2020) and Taquet et al. (2012). Furthermore, in Section 5.3.2, we discuss additional theoretical differences with other astrochemical models to facilitate the understanding of ice-chemistry evolution as well as a guide for future works.

Table 5.3 displays a comparison of the relative ice abundances obtained in our results, normalized to $H_2O$, with related observational and theoretical studies. Boogert et al. (2015) listed ice abundances of securely, likely, and possibly identified observed species in different interstellar objects. Taquet et al. (2012) modeled the formation of the grain mantles during the prestellar core phase and the abundance of formaldehyde, methanol, and radicals. Aikawa et al. (2020) showed the dependence of COMs and warm carbon-chain abundances in protostellar cores on the physical conditions in the prestellar phase via numerical calculations. Taquet et al. (2012) showed similar abundances for $H_2O$ and CO, while in our results, $H_2O$ is hundreds of times more abundant than CO (Figure 5.1). Again, the CO abundance used in their model is chosen initially greater than ours, with a $CO/H \approx 3.0$. Aikawa et al. (2020) obtained a greater difference between water and CO.

Another main difference of the Standard model compared to results from other groups is the higher production of methanol. Knowing that $CH_3OH$ is formed via the hydrogenation of CO, we want to look into the possible link between the high production of methanol and the low production of CO.

## 5.3.2   Sensitivity analysis

We performed a sensitivity analysis to evaluate how molecular abundances vary under parameter variations. For this study, we use the chemical network of the Standard model to study (a) the impact of varying the rate constant ($\Delta k$) and (b) the branching-ratios ($\Delta BR$) on specific formation pathways (gray highlighted processes in Table 5.2). We performed a single simulation run for each variation within the sensitivity analysis, i.e., two runs for reactions 15-16 or reaction 36, and one run for reactions 33-34 and reaction 46. Subsequently, we added 7 surface reactions (green highlighted processes
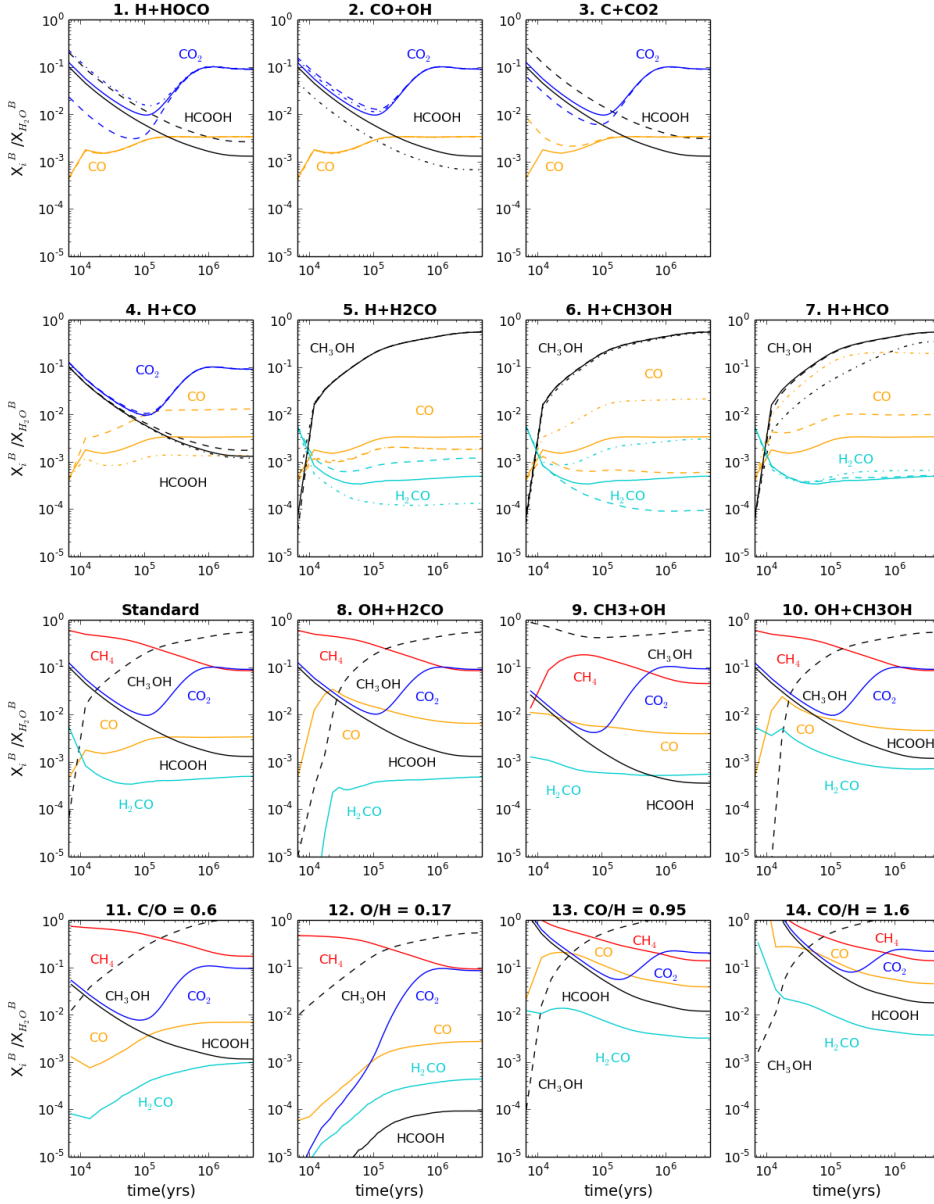
**Figure 5.2:** Grid of figures showing the bulk fractional abundances of the most abundant species relative to water as a function of time in the ice mantle for the Sensitivity analysis. From **1.** to **7.** the standard model (S.) results are shown in full line. **1.** dashed line : forming only HCOOH (BR=0/100), dot-dashed line : forming only $CO_2$ (BR=100/0). **2.** dashed line : forming only $CO_2$ (BR=0/100), dot-dashed line : forming $CO_2$/HOCO 50/50. **3.** dashed line : higher rate. From **4.** to **7.**, dashed lines represent lower rate values than the Standard model, dot-dashed : idem, but higher rates. From **8.** to **14.**, all species are explicitly written respective to each reaction added or ratio modified.

**Table 5.3:** Ice abundances ($/X_{H_2O}$ [%])

| Species | B2015[a] LYSOs | MYSOs | T2012[b] | A2020[c] | C2020[d] | Standard | Opti.(A)[e] | Opti.(B) |
|---|---|---|---|---|---|---|---|---|
| $H_2O$ | 100 | 100 | 100 | 100 | 100 | 100 | 100 | 100 |
| CO | 3-26 | (<3)-85 | 100 | 30.0 | 31.3 | 0.4 | 0.4 | 23.0 |
| $CO_2$ | 11-27 | 12-50 | - | 40.0 | - | 9.0 | 8.9 | 8.8 |
| $CH_3OH$ | (<3)-31 | (<1)-25 | 3.3 | 1.0 | 14.2 | 54.0 | 39.0 | 32.0 |
| $CH_4$ | 1-3 | 1-11 | - | - | - | 8.5 | 8.5 | 8.5 |
| $H_2CO$ | ~ 2 – 7 | ~ 6 | 0.7 | - | - | 0.05 | 0.05 | 0.08 |
| HCOOH | (<0.5)-6 | (<0.5)-4 | - | 0.001 | - | 0.015 | 0.018 | 0.06 |

[a] Boogert et al. (2015)
[b] Taquet et al. (2012) (10K)
[c] Aikawa et al. (2020) (25K)
[d] Chu et al. (2020)
[e] Optimized models as described in section 5.3.3

in Table 5.2) separately, one by one. The total number of runs done is 23, with 16 for the variation analysis and 7 for adding each reaction individually. Furthermore, we tested the variation of C/O, O/H and CO/H ratios, leading to 4 additional simulation runs.

**$CO_2$ and HCOOH formation**

We started the sensitivity analysis by looking into the reactions related to the formation of $CO_2$ and HCOOH (reactions 17-18, 27-28, 29-30, 33-34, 45 and 46).

The reactions that efficiently form $CO_2$ and HCOOH are reactions 17 and 18. By changing the branching ratio for the H+HOCO reaction to exclusively form HCOOH, we see a lack of $CO_2$ before CO freezes out ($<10^5$ years). Nevertheless, the abundance continues to increase until resuming to the original abundance as found in the Standard model (Figure 5.2.1.) due to $CO_2$ gas freezing out ($>10^5$ years). The minor change in the $CO_2$ abundance at a later time is due to OH+CO becoming the main formation pathway (reaction 30). Alternatively, choosing to form exclusively $CO_2$ leads to a complete lack of HCOOH production, showing that reaction 33 does not play a large role in forming HCOOH (Figure 5.2.1.).

As regards the formation of HOCO through reaction 29; when OH and CO are assumed to form only $CO_2$ (reaction 30), the $CO_2$ abundance increases slightly, but again HCOOH is not formed at all, indicating once more the inefficiency of reaction 33 (Figure 5.2.2.). Arasa et al. (2013) found that OH+CO forms a stable HOCO intermediate and $CO_2$, depending on the polarity of the environment and the initial location of CO in the water ice monolayers. However, they conclude that the probability to form HOCO is much greater than to form $CO_2$. The formation of $CO_2$ in our "Standard model" follows this conclusion. Only if the hydrogenation of HOCO is removed from the system, OH+CO can directly form $CO_2$; however, this is unrealistic as the probability of HOCO reacting with H is high in a hydrogenated environment. Yu et al. (2005) suggested the importance of the direct formation of $CO_2$ via OH+HOCO (reaction 47) in a gas-phase simulation in an atmospheric environment. Adding this reaction to our model does not modify our results and the different settings do not allow us to extrapolate the importance of OH+HOCO in solid-state simulations.

An alternative formation pathway to $CO_2$ is the solid-state reaction of C with $O_2$ (Qasim et al. (2020b)). Based on their experimental results, this reaction is found to be a minor sink for $O_2$ consumption in the translucent and dense phases of interstellar clouds. In our model, we do not observe any differences by changing the branching-ratio of reaction 27 and 28. Furthermore, Qasim et al. (2020b) also considered the reaction $C+CO_2$ with a high activation barrier, leading to a low rate constant, as shown in Table 5.2, reaction 46. To test the importance of this reaction, we increased the rate constant. Further depletion of $CO_2$ by the atomic carbon, leads to a higher amount of CO and a lower amount of $CO_2$, before CO-gas and $CO_2$-gas freeze-out ($<10^5$ years) (Figure 5.2.3.). After the freeze-out period the surface chemistry is restored as in the Standard model. While HCOOH is increased homogeneously throughout the cloud

evolution, due to the reaction 29 becoming predominant.

**H$_2$CO and CH$_3$OH chemistry**

To look into the high amount of methanol and a low amount of CO found in the Standard model, we varied the rate constant and BR of the reactions involved in the methanol formation pathway (reaction 36 → 16 → 38 → 13). Note that all rate constants are taken from computational chemical literature and are rather well-constrained, hence we vary the rate constants only within an order of magnitude.

**Rate constant: H + CO → HCO**   The rate constant implemented in the Standard model is from Andersson et al. (2011). By increasing the rate constant of reaction 36, from $10^4$ s$^{-1}$ to $10^5$ s$^{-1}$, we observed that the CO abundance decreases while CO$_2$ and HCOOH vary, see Figure 5.2.4. The changes in the abundance profiles are simply due to the fact that CO is being depleted by atomic hydrogen (H+CO), which secondarily impacts CO$_2$ and HCOOH abundances, since these abundances are dependent on the CO+OH reaction (reactions 29 → 17-18).

**H + H$_2$CO → products**   Song & Kästner (2017) investigated the hydrogenation reactions of H$_2$CO, which yields CH$_3$O and CH$_2$OH, and the hydrogen abstraction reactions, which result in H$_2$+HCO on an amorphous solid water surface. They validated a significant contribution of quantum tunneling at low temperature, and the calculated rate constant confirmed that the channel leading to CH$_2$OH is negligible. When the rate constants of reaction 37 and 38 are varied, only H$_2$CO and CO are affected, and all other species remained unchanged (Figure 5.2.5.). We can clearly see H$_2$CO being depleted when the rate is increased, but CO is moderately impacted due to the loop reaction, HCO-CO (reactions 36 and 15). Methanol remains unchanged due to the formation of CH$_2$OH becoming non-negligible (reaction 39 → 7) compensating the lack of CH$_3$O. Which means by decreasing the rate constants, CH$_2$OH becomes more available than CH$_3$O and the abundance of CH$_3$OH, because of the formation pathway H+CH$_2$OH, remains high. But if the rate constants are increased, CH$_3$O becomes more abundant and CH$_3$OH continues to be formed via reaction 14.

**H + CH$_3$OH → products**   Cooper & Kästner (2019) have studied the kinetics of H + CH$_3$OH → H$_2$ + CH$_2$OH and provided rate constants relevant to surface reactions down to temperatures as low as 25 K. When we increase the rate of this reaction, methanol slightly decreases, and CO and H$_2$CO increase (Figure 5.2.6.). When CH$_2$OH is hydrogenated, reverse reactions can happen, leading to the formation of H$_2$CO (reaction 8), then H+H$_2$CO can also form HCO (reaction 37), and H+HCO can form CO (reaction 15). The small depletion of methanol allows these reverse reactions coming from CH$_2$OH (reaction 8 → 37 → 15) to become more efficient. This illustrates the need to include more destruction pathways in the standard model.

To summarize this first part of analysis, as the model in this work includes the most recent chemical networks with values that were not previously available for past astrochemical models, we assess the accuracy of the results but the number of free parameters are severely limited, leaving us only a small window for parameter variations and testing. Although, by analysing the sensitivity of these reactions with different superficial rate constants, we observed the importance of reverse reactions contributing to the formation of smaller species. Radicals, like HCO, could be a key reactant material for even bigger COMs (Chuang et al. (2016); Lamberts et al. (2019)).

**BR: H + HCO → products**    The branching-ratio of reaction 15 and 16 were chosen from the estimated values of Simons et al. (2020). They used electronic structure calculations to determine the branching ratio of several chemical reactions. Their work is the first to report branching ratios in the literature, serving as a guide for the major and minor product channels of radical-radical reactions. Although much can be learned from the applied density functional theory (DFT), additional insights can be obtained. Kayanuma et al. (2019) performed an extended study of HCO+H on a graphene surface via ab initio molecular dynamics (AIMD) simulations, analyzing the formation and desorption of organic molecules on the dust surfaces in the interstellar medium. They concluded that when a free atomic hydrogen reacts with the HCO chemisorbed at the C atom, $H_2CO$ is not generated (reaction 16).

Therefore, recognizing these two conclusions, we choose to favor the formation of CO (reaction 15) over $H_2CO$ (reaction 16) and see the impact on the entire ice chemistry. We decided to gradually increase the CO:$H_2CO$ ratio from 58:42 (Simons et al. (2020)), used in the Standard model, to 80:20 and an extreme case 98:2 (Figure 5.2.7.). The first observation is the strong influence of reaction 15 over the CO abundance profile. Concerning that $CO_2$, HCOOH and $H_2CO$ are heavily linked with CO, all three molecules have a moderate increase in abundance as well. The $CH_3OH$ abundance profile drops to an unexpected level, even lower than CO profiles, but only if the branching ratio is greater than 95:5, which reduces the efficiency of $CH_3OH$ formation pathways through the hydrogenation of CO-HCO-$H_2CO$-$CH_3O$. Following a closer idea with Kayanuma et al. (2019), changing the branching ratio to 98:2, leads to fractional abundances ($/X_{H_2O}[\%]$) comparable to recent observations, see Table 5.3. Then by changing strongly the branching ratio of reaction 15 and 16, the model shows CO+H formation pathway to become minor reactions into the system and methanol to be strongly depleted. In that case, other formation pathways would need to be included if a higher amount methanol is to be expected. Otherwise, with a 58:42 ratio, $CH_3OH$ is highly abundant, efficiently formed via CO+H pathways. We show in the following paragraphs other possible ways to increase CO/$CH_3OH$ ratio but we suggest further extended study on these reactions due to their high impact on the methanol chemistry.

Continuing to analyse the methanol chemistry and the formation pathway possible in a dense cloud environment, we added separately five reactions of interest at low temperature, which are discussed below.

**New reaction: OH + H$_2$CO → HCO + H$_2$O**     Zanchet et al. (2018) showed low temperature dynamics of this reaction. Using their recent theoretical results, we added OH+H$_2$CO to the surface chemistry. In our case, adding this reaction changed the abundance profiles of CO, H$_2$CO and CH$_3$OH (Figure 5.2.8.). In addition to the hydrogenation of H$_2$CO (reactions 37 to 39), we see H$_2$CO also strongly depleted by OH (reaction 38) at an early time, which influences the CH$_3$OH abundance profile. H$_2$CO and CH$_3$OH recover over time due to the hydrogenation of CO (reaction 36 → 16 → 38 →13). We find that the reaction OH+H$_2$CO is an efficient destruction pathway for formaldehyde before the freeze out period, competing with H+H$_2$CO.

**CH$_4$ + OH → CH$_3$ + H$_2$O and CH$_3$ + OH → CH$_3$OH**     Lamberts et al. (2017) were the first to provide rate constants at temperatures down to 65K for the CH$_4$+OH reaction. This is added to our surface chemistry as reaction 49. In a subsequent work, Qasim et al. (2018) showed experimentally the formation of methanol by the sequential reaction chain, CH$_4$+OH → CH$_3$+H$_2$O and CH$_3$+OH → CH$_3$OH at 10-20K. By adding these reactions to the Standard model, all species are influenced in our model (Figure 5.2.9.). The dominant change that impacts the rest of the chemistry is the strong depletion of solid-state CH$_4$ before CH$_4$ gas freezes out ($<10^5$ years). Then at earlier time, due to OH being consumed by CH$_4$, the OH+CO reaction becomes less probable, therefore resulting in lower CO$_2$ and HCOOH abundances (see reactions 29-30). On top of seeing changes with the abundance profiles, we noticed CH$_3$+OH reaction (reaction 35) to be the main formation pathway of methanol until CO freezes out and overtime CO+H formation pathway (reactions 36 → 16 → 38 → 13) becomes more efficient. That is why CH$_3$OH is produced highly, compared to the Standard model, at earlier time.

**CH$_3$O + H$_2$CO → CH$_3$OH + HCO**     Álvarez-Barcia et al. (2018) studied the efficiency of this reaction in comparison to other radical-neutral reactions as well as to fast barrierless radical-radical reactions. They calculated activation and reaction energies using DFT techniques. Subsequently, Simons et al. (2020) concluded that the most important reaction leading to methanol is H$_2$CO+CH$_3$O → HCO+CH$_3$O, i.e. more relevant than through the 4$^{th}$ hydrogenation step in the CO+H chain. By adding this reaction only to our Standard model we did not observe an impact to the abundance profiles or changes in the main formation pathways. Regardless, as can be seen in Section 5.3.3 (Opt. A), by combining other radical-neutral and radical-radical reactions, favoring the production of CH$_3$O or H$_2$CO, we can compare with the results of Simons et al. (2020) and see CH$_3$O+H$_2$CO → CH$_3$OH + HCO becoming noticeable over time.

**OH + CH$_3$OH → products**     Ocaña et al. (2019) showed experimentally and theoretically reactions 51 & 52 being fast and effective routes to CH$_2$OH and CH$_3$O at the low pressures and temperatures prevalent in the interstellar medium. By adding

these reactions, when compared to the Standard model, $CH_3OH$ is formed later on and $H_2CO$, CO become more abundant before $2.0\times10^4$ years (Figure 5.2.10.). The strong depletion of OH due to the reaction with the abundant $CH_3OH$, allows minor reactions with OH to be diminished (reactions 33 and 34), leading to more available HCO in the system. After CO-ice freezes out, the chemistry is resumed to a high $CH_3OH$ and low CO. Adding this methanol destruction pathways (reactions 51 and 52) has an effect on the chemistry, but by itself, it is minor compared to slowing down the efficient CO+H formation pathway (reaction 36 → 16 → 38 →13). More molecules interacting with HCO, $H_2CO$, $CH_3O$ and $CH_2OH$ need to be included into the ice chemistry.

**O/H, C/O and CO/H ratios**

Following the results presented in the sensitivity analysis, we decided to vary the initial carbon reservoir and the initial amount of hydrogen in order to see the impact of these ratios on the ice chemistry. We compared our results to other theoretical studies and checked the influence on $CH_3OH$ overproduction. We kept the physical parameters ($T, n, A\nu, \zeta$) appropriate for a dense cloud environment.

Concerning the C/O ratio, our initial value is 0.4. Unless the carbon initial abundance is assumed to be larger than that of the oxygen, the ice chemistry will not be significantly changed. As shown in Figure 5.2.11, decreasing the amount of oxygen (C/O ratio = 0.6) leads to variations in the abundances, but does not change the overall results. On the other hand, when varying the O/H ratio initially equal to 1.7, changes in the ice chemistry become drastically noticeable. If more hydrogen is included in the system (O/H = 0.17), all species are depleted, except for $CH_4$ and methanol having higher abundance profiles. All formation pathways by hydrogenation become more effective, explaining the depletion of CO-species and the increase of $CH_4$ as well as $CH_3OH$ (reactions 9 → 12, reaction 36 → 16 → 38 → 13). After $10^5$ years, all species, besides HCOOH, recover showing similar abundance profiles as in the Standard model (Figure 5.2.12). The difference with HCOOH is due to insufficient available OH in the system. The radical is consumed rapidly by hydrogen beforehand (reaction 4 → 5), leaving OH+CO reaction forming HCOOH and $CO_2$ less efficient. $CO_2$ recovers well due to the freeze out of $CO_2$-gas compensating the inefficiency of OH+CO. As regards, the CO/H ratio, we started our simulations without CO initially present in the gas-phase. As described in Section 5.2.2, we estimated the carbon to be stored as atomic carbon until $10^4$ years. Simons et al. (2020) and Taquet et al. (2012), chose even denser environments, with C stored in CO from the start. To show the possible difference in the ice chemistry depending on this parameter, we included CO as an initial species. First, (a) we used a similar CO/H ratio < 1.0, as Taquet et al. (2012). Second, (b) we used a CO/H ratio > 1.0, as Simons et al. (2020). Figure 5.2.13 and 5.2.14 show the results obtained for both cases. Including CO initially allows H+CO/H+HCO to be favored over H+OH, leading to all species abundances to increase besides water being depleted. As for the $CO/CH_3OH$ ratio, case (a) shows a ratio of 0.027, while Taquet et al. (2012) obtained 0.3. In case (b), we have

CO/CH$_3$OH = 0.033, while Simons et al. (2020) obtained 16.06. Hence, including an initial non-zero CO abundance in the Standard model leads to some differences in the chemistry but does not reduce the overproduction of methanol.

## Summary

Based on the model presented here, including new reaction pathways and updated reaction constants, as well as the performed sensitivity analysis, we find :

- Irrespective of variation of rate constants and branching ratios, the main formation pathway of methanol in the Standard model is through the hydrogenation of CO.

- However, adding reactions 49 and 35 to the Standard model, we see the chemistry changes and reaction 35 become the main formation pathway of methanol before CO freezes out.

- Although we included additional reactions, we found the CO/CH$_3$OH ratios to be too low with respect to observational results. This is a robust result since the relevant rate constants are known to high accuracy.

- While the assumed initial elemental conditions can significantly change the computed overall ice composition, increasing the CO/H ratio does not regulate the high amount of methanol.

- The adjustable parameter found to have a strong impact on the methanol chemistry is the branching ratio of the H+HCO reaction. We find that this value is crucial for controlling methanol formation through the hydrogenation route.

## Remarks

On the theoretical side, our comparisons with Taquet et al. (2012), Simons et al. (2020) and Aikawa et al. (2020) are complementary discussions for COMs studies, on grain surfaces, at low temperature. Taquet et al. and Aikawa et al. can be closely compared to each other due to the rate method applied throughout their research, while Simons et al. and we use kMC method. Regardless using the same method to calculate the chemical abundances of each species overtime, we differ in few important points leading to unequal results. As discussed previously, we do not have the same initial CO abundance, but other factors need to be mentioned. First, the chemistry used by Simons et al. include larger molecules, containing up to 10 atoms, whereas the largest in our surface network is CH$_3$OH. For example, in Simons et al. HCOOCH$_3$ (methylformate, MF) is formed through HCO+CH$_3$O, and once it is formed, there is no destruction reaction included. As explained above, we find that the hydrogenation of CH$_3$O is a main route to CH$_3$OH, but in Simons et al. it is also destroyed in forming MF and other large organic molecules, lowering the probability

of forming $CH_3OH$. In addition, we also include only four tunneling reactions which destroy $CH_3OH$ by hydrogenation (reactions 40-41) and by OH (reactions 51-52). Second, diffusion, desorption and accessibility of the species are fully positional.

Furthermore, a few possible, but complex, points could be improved to decrease the uncertainties on the results and obtain better comparison with observations. One is including the binding energies specific for each species in the stochastic method. Second is a more accurate calculation of the H+HCO branching ratios on different ice surfaces. Both involve vigorous theoretical and computational studies.

All combined remarks and results given throughout the paper provide a clear guide for future models, decreasing the overall uncertainties of the simulations and showing extended explanation of the chemistry evolution's.

### 5.3.3   Optimized models

Analyzing all simulations, we constructed optimized models for a dense cloud environment to better compare with observed ice mantle abundances (Table 5.3), but without compromising the accuracy of the updated model. We decided to include all chemical reactions listed in Table 5.2 with no changes in any rate constant from the Standard model. Figure 5.3 shows the results of the optimized models for different H+HCO branching ratios: (A) 58:42 (Standard) and (B) 98:2; as done for the sensitivity analysis model in Section 5.3.2.

(A) - Adding all the radical-neutral and radical-radical reactions to the model shows significant changes to ice chemistry. First, the depletion of $CO_2$ and HCOOH due to the consumption of OH by the reaction, $CH_4$+OH. $CO_2$ is replenished to a similar level as in the Standard model after $CO_2$ gas freezes out. Linked to this, CO becomes more abundant because of less OH available to react with CO (reaction 29-30). Regarding $CH_3OH$, the abundance profile starts increasing later than in the Standard model, but remains the second main species over time ( $2.0 \times 10^5$ years). For the chemistry analysis, we see $CO_2$ and HCOOH still dominantly formed by the two-step reactions, OH+CO and then H+HOCO, similarly as in the Standard model. In the case of $CH_3OH$, before CO freezes out, $CH_3$+OH is the main formation pathway and afterwards the hydrogenation route takes over, as seen previously in the sensitivity analysis (Section 5.3.2). However, H+$CH_2OH$ becomes the major reaction to form methanol over the reaction, H+$CH_3O$, due to the efficient depletion of $CH_3O$ via reaction 50, leading to less $CH_3O$ in the system. Furthermore, the reaction $CH_3O$+$H_2CO$ becomes more efficient over time. The abundance ratios are compared in Table 5.3.

(B) - Increasing the branching ratio of the reaction, H+HCO, shows the dramatic impact on the CO and $CH_3OH$ evolution and the resolution of the $CH_3OH$ overproduction issue. CO becomes one of the major species, competing with $CH_3OH$ overtime. The abundance profile of methanol slowly increases until $10^5$ years, in which the change in the abundance eventually reaches a stationary state. The "step" seen in $H_2CO$ and $CH_3OH$ profiles (lower right panel of Figure 5.3) is due to the freeze-out of CO around this time period, which rapidly reacts with atomic hydrogen. For the

CO/CH$_3$OH ratio, we obtain our highest value of 0.72, i.e the CO/CH$_3$OH ratio is two times less than in Chu et al. (2020) and twenty-times less than in Simons et al. (2020). But if we look into Table 5.3, by comparing all ice abundances (/X$_{H_2O}$[%]) with observational and theoretical works, we obtain close ratios. The major formation pathways of each species are unchanged from those described above in the previous case. The unique difference is CH$_3$O+H$_2$CO becomes overall less effective than in case (A).

## 5.4   Astrophysical implications

Previously mentioned, Chu et al. (2020) have simultaneously measured the CO and CH$_3$OH ice features for background targets in dense cores. After observing the spectra of different dense molecular cores, they found conversion of CO ice into CH$_3$OH ice to be sufficient to explain the CH$_3$OH ice that is detected towards low mass Class 1 YSO envelopes. They do not directly observe complex organic molecules (COMs), but expect the high CO to CH$_3$OH conversion rate to lead towards the formation of COMs before the development of a star, depending on the efficiency of methanol formation under cold conditions without energetic processing. One clear finding of this paper is the effectiveness of CO to CH$_3$OH conversion on the grain surface chemistry at low temperature (10K). As discussed throughout the paper and shown in Table 5.3, we obtained a high amount of CH$_3$OH, even a higher ratio than Chu et al. (2020) and on the upper-end of Boogert et al. (2015). However, the environments where ice is detected can affect the efficiency of the CO to CH$_3$OH ice conversion where factors such as CO freeze-out (Boogert et al. (2015)), dust densities and temperatures play a role.

Another finding in our research is the importance of reactions such as CH$_3$+OH and CH$_3$O+H$_2$CO in the optimized model, showing to be highly effective formation pathways of methanol throughout the cloud evolution. In summary, not only CH$_3$OH can efficiently being formed on the grains in the dense, cold and no-radiation phase of an interstellar cloud, through hydrogenation of CO, but radical-radical reactions or radical-molecule reactions are effective. As mentioned by Boogert et al. (2015) and observed by other research groups (Dartois et al. (1999); Pontoppidan et al. (2003); Cuppen et al. (2011); Penteado et al. (2015)), processing simple ices by UV photons leading to CH$_3$OH formation is not efficient enough to explain the enhanced abundances toward massive YSOs and even less for low-mass YSOs. Our model, combined with all calculated rates and recent experiments (Table 5.2), provides a better understanding of these abundances (Table 5.3).

As commented in the introduction, future high angular resolution ground and space-based (James Webb Space; JWST) infrared facilities promise great advances of ice studies. They will enable ice studies in extreme environments (strong radiation fields, high or low metallicities) together with further understanding of molecule formation pathways. Currently, not even methanol has been directly and exclusively
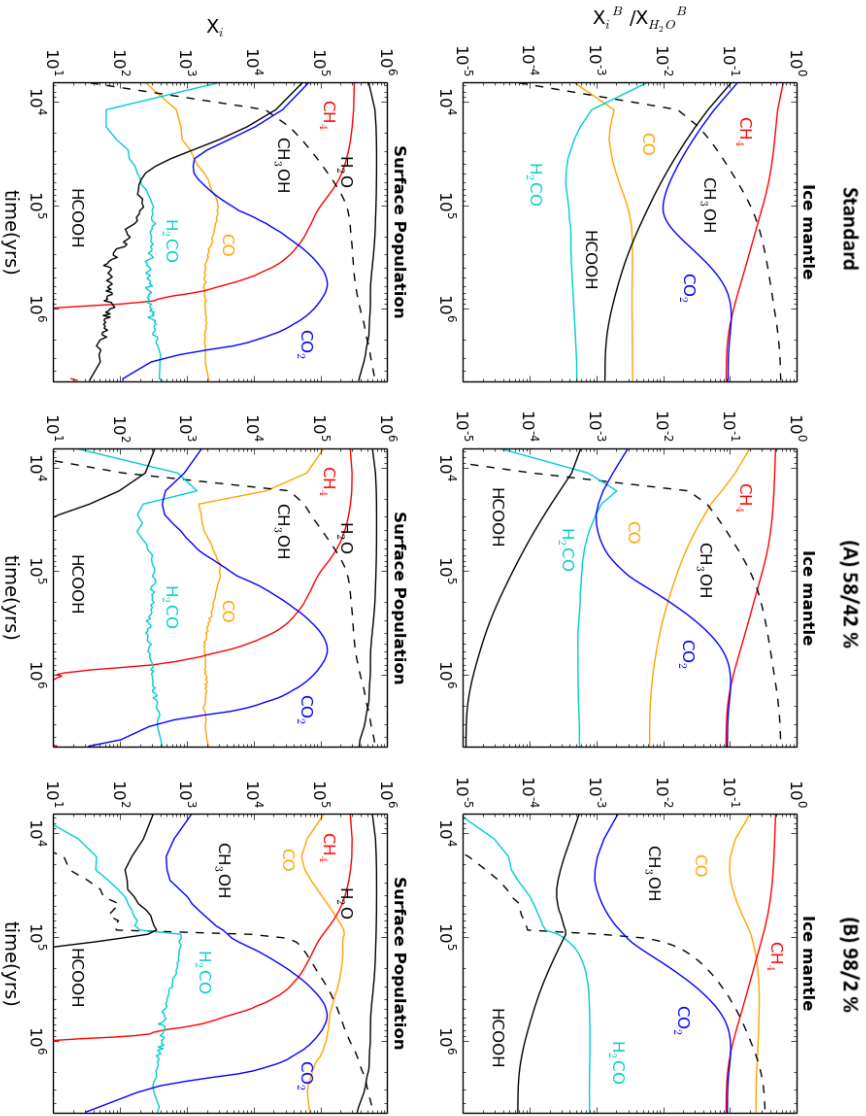
**Figure 5.3:** Ice chemistry of the Standard model compared to the optimized models (A) and (B) as a function of time.

detected in the polar phase of the cloud (H/H$_2$ ratio >1; A$\nu$ < 3). JWST will provide a much larger understanding of COMs and ice growth throughout the cloud evolution and even further into the life cycle of a star. By comparing the amount of ices observed with model predictions, as done in this paper, it will allow to comprehend the ices complexity.

## 5.5  Conclusions

We developed an astrochemical model containing an updated chemistry in a dense cloud environment, calculated by a stochastic method. We extensively analysed the formation/destruction pathways of several molecules important in the interstellar medium, i.e. H$_2$O, CH$_4$, CO$_2$, HCOOH, H$_2$CO, CH$_3$OH. We compared our results to recent observations and theoretical works in order to validate our model and to discuss future improvements. We can summarize our main results in a few points:

- HCO plays a major role in CO and CH$_3$OH chemistry through the reaction, H+HCO. By changing the branching ratio of this reaction, i.e., to favor the formation of CO over H$_2$CO, we see CO becoming highly abundant overtime and the formation of methanol, through the hydrogenation pathway, being diminished.

- We created an optimized model from the results of the sensitivity analysis. We added several efficient reactions to the Standard model, while keeping the accuracy of the rate constants. As shown in Table 5.3, the abundance ratios are in a close agreement with recent theoretical and observational results.

- We show that in a H$_2$O-rich ice environment, methanol is formed predominantly by CH$_3$+OH at early times, and afterwards being mainly formed by the hydrogenation pathway. This is in line with recent laboratory studies and upcoming observational work.

Our results give insights on the product channel of smaller COMs at low temperature throughout the cloud evolution. Furthermore, this paper provides an elaborate "guide" for future models, concerning the accuracy of the chemical network and the kinetic Monte Carlo simulations, the impact of the initial conditions and finally shows the need of further calculations of rate constants and BR on different ice-surfaces. Further points of interest are to add H$_2$ reactions and bigger COMs, as well as to vary the cloud environment by adding UV-radiation.